IOP Conference Series: Materials Science and Engineering

Measurement techniques for liquid metals

To cite this article: M Ratajczak *et al* 2017 *IOP Conf. Ser.: Mater. Sci. Eng.* **228** 012023

Measurement techniques for liquid metals

M Ratajczak[1], D Hernández[2], T Richter[3], D Otte[4], D Buchenau[5], N Krauter[1], T Wondrak[1]

[1] Helmholtz-Zentrum Dresden - Rossendorf (HZDR), Institute of Fluid Dynamics, Bautzner Landstraße 400, 01328 Dresden, Germany
[2] Institute for Thermodynamics and Fluid Mechanics, Technische Universität Ilmenau, 98684 Ilmenau, Germany
[3] Institute of Fluid Mechanics, Chair of Magnetofluiddynamics, Measuring and Automation Technology, Technische Universität Dresden, 01069 Dresden, Germany
[4] Institute of Thermal Process Engineering, Karlsruhe Institute of Technology, 76131 Karlsruhe, Germany
[5] HZDR Innovation GmbH, Bautzner Landstraße 400, 01328 Dresden, Germany

E-mail: `t.wondrak@hzdr.de`

Abstract. The measurement of flow properties of liquid metals, such as flow rate, flow structure and gas distribution, is a challenging task due to the opaqueness, the high temperatures (e. g. 1500 °C for liquid steel or liquid silicon) and the corrosiveness of those fluids. In this paper, a short review about the recent developments of measurement techniques in the framework of the Helmholtz Alliance Liquid Metal Technologies (LIMTECH) is presented. It focuses on the development of contactless inductive measurement techniques exploiting the high electrical conductivity of those melts. These measurement techniques include the contactless inductive flow tomography (CIFT), which is able to reconstruct the mean three-dimensional velocity structure in liquid melts, local Lorentz force velocimetry (local LFV), which enables the local assessment of flows close to the wall, and inductive methods for bubble detection, which are based on mutual inductance tomography (MIT). Additionally, a short overview of contactless inductive flow rate measurement techniques is given. Furthermore, an ultrasound technique called ultrasound transit-time technique (UTTT) will be presented which enables the measurement of position and size of bubbles in large vessels.

1. Introduction

In many industrial applications, flow properties of hot liquid metals play an important role for the processes. Sodium or lead alloys are used as coolants for nuclear power reactors or for solar power stations. Important parameters are the flow rate and the existence of bubbles. In metallurgy, gas is injected into the melt at various stages of melt refining, e.g. for carbon reduction or stirring [1]. Thus, detailed knowledge about the flow structure, the void fraction, the trajectory and the size of bubbles helps to understand and to control the process. A very complex flow regime can be found in the submerged entry nozzle (SEN) and in the mold of a continuous caster of steel, which is operated at about 1500 °C. The flow structure of liquid steel in the mold plays an important role for the quality of the product, because it influences the forming of surface defects and inclusions [2]. Often argon gas is injected into the SEN in order to reduce nozzle clogging and to catch impurities in the melt. Similarly, in the production of mono-crystalline silicon for electronic devices or solar cells, the flow of the liquid silicon in the crucible below the crystallization front is important. For instance, the flow structure has an effect on the number of defects and the concentration of oxygen in the produced crystal. Last but not least, a liquid metal reactor filled with liquid tin is used for cracking of methane and ethane into hydrogen [3]. The operating temperature is in the range of 800 °C to 1200 °C.

Due to the high temperature and the corrosiveness of those melts, contactless methods are preferred. However, well established contactless optical methods like particle image velocimetry or laser Doppler anemometry are precluded due to the opaqueness of the melts. For this type of fluids, ultrasonic measurement techniques can be used. Ultrasound Doppler velocimetry (UDV) [4] measures the flow profile along the ultrasound beam generated by the transducer using scattering particles in the fluid. When the transducer is in direct contact with the fluid, this technique is limited to temperatures of around 200 °C. With the help of wave-guides it is possible to adapt the transducer to temperatures of up to 600 °C due to the increased distance between the transducer and the melt [5]. Ultrasound can also be used to measure the trajectory and the size of bubbles by means of the ultrasound transit-time technique (UTTT) [6]. The advantage of this technique is the applicability to a large fluid volume, while radiation based techniques, such as neutron [7] or X-ray radiography [8], are limited regarding the thickness of the vessel due to the high attenuation of the rays by the liquid metal.

A different type of contactless measurement techniques exploits the high electrical conductivity of metallic melts by using the principle of induction. Typically, a contactless measurement device applies an externally generated magnetic field to the fluid and detects the perturbations of that magnetic field caused either by the change of the electrical conductivity in the volume or by the movement of liquid metal through the magnetic field. The first induction principle can be exploited for level or bubble detection and is the key principle of the mutual inductance tomography (MIT), which is able to detect the conductivity distribution in one cross section of a pipe [9]. The latter one can be used to measure flow rate like the phase shift flow meter [10] or the Lorentz force velocimetry (LFV) [11]. There exist also measurement techniques that are able to resolve the spatial distribution of the flow. One of these is contactless inductive flow tomography (CIFT) [12], which measures the perturbation of the applied magnetic field with magnetic field sensors distributed around the melt. The three-dimensional mean flow structure in the melt is then reconstructed by solving a linear inverse problem.

Additionally, LFV can be extended to detect the flow structure close to the wall by using a permanent magnet whose dimensions are significantly smaller than that of the flow. Only a small volume of the melt is penetrated by the magnetic field and the velocity in this region contributes to the signal. By placing the sensor consecutively at different positions along the wall, the spatial distribution of the force on the magnet is measured which depends on the spatial distribution of the flow velocity close to the wall. This technique is called local Lorentz force velocimetry (local LFV) [13].

A more detailed overview of measurement techniques for liquid metals including invasive probes, such as Vives probes for velocity measurement or resistivity probes for bubble detection, is given in the LBE handbook [14].

This paper will review the research conducted on the development of measurement techniques in the framework of the Helmholtz Alliance Liquid Metal Technologies (LIMTECH). In the beginning, a brief overview of inductive flow rate measurement techniques is given in section 2. This includes not only the new immersed eddy current flow meter (see section 2.2), the transient eddy current flow meter (see section 2.3) and advances in LFV (see section 2.5), but also well established methods such as the phase shift sensor (see section 2.1) or rotary flow meters (see section 2.4) are shortly described for the sake of completeness. The main focus of the work in LIMTECH was the development of the measurement techniques presented in the next sections: local Lorentz force velocimetry (see section 3), contactless inductive flow tomography (CIFT) (see section 4), ultrasound transit-time technique (UTTT) (see section 5) and inductive methods

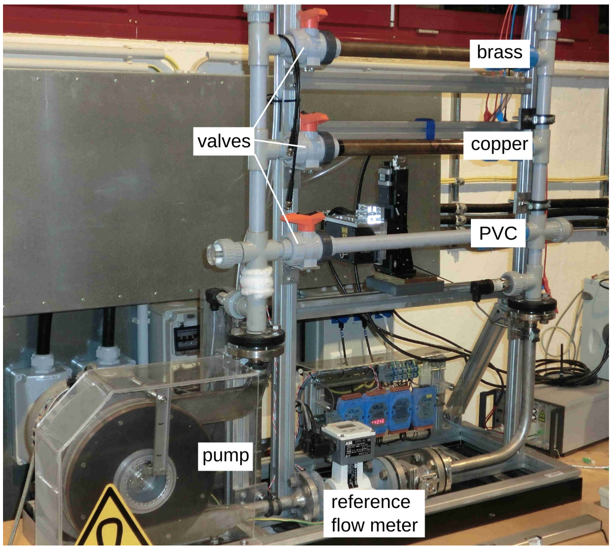

Figure 1. Photo of the GaInSn loop with the pump, the reference flow meter and three different sections made of PVC, brass and copper.

for bubble detection based on the principle of MIT (see section 6). The paper is concluded with a short description of a new level measurement system (see section 7).

2. Inductive flow rate sensors

All flow rate sensors presented in this section were tested at the liquid metal loop seen in Figure 1 which is operated with the eutectic alloy GaInSn at room temperature. The lower part of the loop consists of a circular stainless steel tube with the inner diameter $D = 27\,\mathrm{mm}$. The upper part consists of three independent test sections with a length of 400 mm each. The test sections can be opened and closed independently by valves. They are equipped with three pipes made of brass, copper and PVC which have the same inner diameter as the stainless steel tube in the lower section. The melt is driven by a permanent magnet induction pump with a maximum mean velocity of about $1.5\,\mathrm{m\,s^{-1}}$. As reference, the commercially available flow meter (Copa XL DN25) from ABB is used.

We start with a short description of the phase shift sensor (see section 2.1) and the newly developed eddy current flow meter (ECFM), which is an immersed version of the phase shift sensor (see section 2.2). The next presented sensor is the newly developed transient eddy current flow metering (TEC-FM) sensor, which is available as an external and an immersed sensor (see section 2.3). The advantage of TEC-FM is that it is calibration free. The section is concluded with the description of flow meters which are based on flow induced forces on permanent magnets: the rotary flow meter, the magnetic fly-wheel (see section 2.4) and the Lorentz force velocimetry (see section 2.5).

Before the different flow rate sensors are presented, we shortly delineate the basic principle of inductive flow measurement techniques which is is Ohm's law for moving conductors

$$\vec{j} = \sigma_l(\vec{u} \times \vec{B} - \nabla\phi)\ . \tag{1}$$

If a static magnetic field $\vec{B}$ is applied to the fluid domain with conductivity σ_l, the current $\vec{j}$ in the fluid depends on the flow field $\vec{u}$, the magnetic field $\vec{B}$ and the gradient of the induced electric potential ϕ. The current $\vec{j}$, in turn, generates a flow induced magnetic field $\vec{b}$ which is called the secondary magnetic field. Therefore, the magnetic field $\vec{B}$ is in general the sum of an

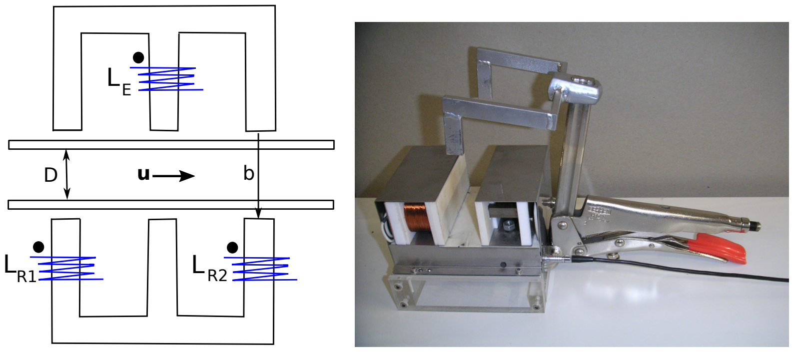

(a) (b)

Figure 2. Schematic diagram (a) and photo (b) of the phase-shift flowmeter with the emitting coil L_E and the receiving coils L_{R1} and L_{R2} around the pipe with the diameter D.

externally applied primary magnetic field $\vec{B}_0$ and the induced secondary magnetic field $\vec{b}$. The ratio between $\vec{b}$ and $\vec{B}_0$ is proportional to the magnetic Reynolds number, defined as

$$\mathrm{Rm} = \mu_0 \sigma_l l u \ , \tag{2}$$

with μ_0 representing the magnetic permeability of vacuum and l and u denoting characteristic length and velocity scales of the flow, respectively. Typically, in most industrial application Rm is smaller than 1 so that the influence of $\vec{b}$ can be neglected.

The electric potential ϕ can be obtained by taking the divergence of Equation (1) and solving the emerging Poisson equation

$$\nabla^2\phi = \nabla \cdot (\vec{u} \times \vec{B}). \tag{3}$$

The current $\vec{j}$ in the fluid volume generates not only the secondary magnetic field $\vec{b}$ but also under the influence of the magnetic field $\vec{B}$ the Lorentz force density $\vec{f}$ in the fluid

$$\vec{f} = \vec{j} \times \vec{B} \ . \tag{4}$$

The Lorentz force can be used to control the flow in the melt or to measure the flow by means of LFV (see section 2.5) and local LFV (see section 3).

2.1. Phase-shift sensor

The phase-shift sensor is based on a transformer principle operating without any locomotive parts. This contactless AC flow rate sensor can be realized in a lateral and an axial arrangement of the coils. The detector head of the lateral phase-shift sensor (cf. Figure 2) consists of two receiving coils and an emitter coil, placed on opposite sides of the duct containing the liquid metal flow. The emitter coil L_E is fed by a temperature stabilized alternating current I of constant frequency f [10, 15, 16]. In order to minimize the magnetic stray field of the sensor and to enlarge the signal quality, all coils are interspersed with laminated mild iron providing a low magnetic resistance of the sensor arrangement. An alternating magnetic flux is provided by the emitter coil perpendicularly orientated to the flow direction of the electrically conductive melt.

A symmetrical adjustment of the sensor arrangement is achieved for the case that the emitter coil flux is distributed half-and-half over both receiver coils. In order to adjust the symmetry of the sensor, the conductive melt has to be at rest. Considering a symmetrical arrangement of the emitter L_E and receiving coils L_{R1} and L_{R2}, the equal distribution of the alternating magnetic flux is disturbed by the movement of the conducting flow. The information about the averaged

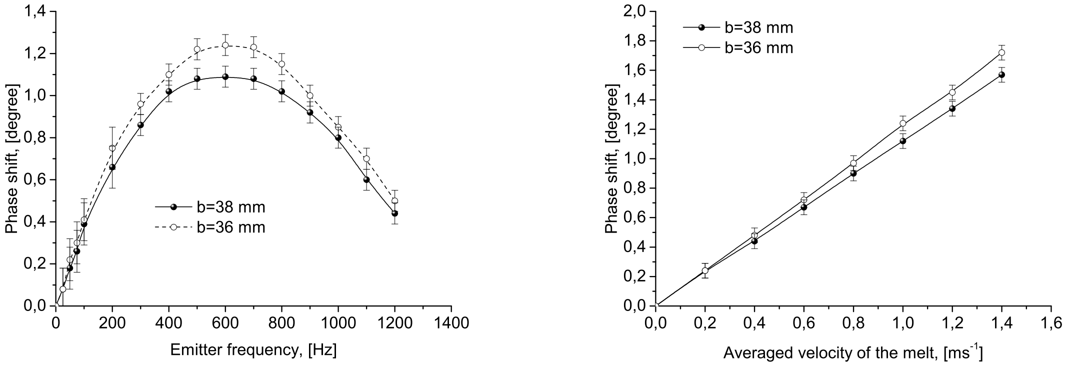

(a) (b)

Figure 3. Frequency response (a) at $u_0 = 1\,\mathrm{m\,s^{-1}}$ and flow induced phase-shift (b) in dependence of the mean velocity measured at the PVC test section for an emitter frequency of $f = 600\,\mathrm{Hz}$ (cf. [15]).

velocity u_0 or flow rate Q is provided by a voltage difference U_D or phase-shift $\Delta\phi$ between the receiver coils. The dependence between the phase-shift and the velocity is given by following function g

$$\Delta\phi = g\left(f, Rm, K\right) \ . \tag{5}$$

The measured effect is proportional to the magnetic Reynolds number Rm. The flow rate sensor has to be calibrated as indicated by the factor K in Equation (5). Some comparable measurements of the flow-induced phase-shift in dependence of the flow profile at an emitter frequency of $f = 600\,\mathrm{Hz}$ are shown in Figure 3 for two different widths of the coil gap $b = 38\,\mathrm{mm}$ and $b = 36\,\mathrm{mm}$. The results shown in Figure 3(a) indicate that the optimal frequency is about 600 Hz. The phase-shift measurements seen in Figure 3(b) show again a very good linearity with the averaged velocity in the duct.

An alternative realization of an AC electromagnetic flowmeter has been suggested by Schulenberg et al. [16], which is illustrated in Figure 4. The flowmeter consists of two emitter or sending coils L_{E1} and L_{E2} which are supplied with alternating electric currents I_{LE1} and I_{LE2} in opposite direction [10, 15, 16]. The arrangement of emitter coils is comparable to an Anti-Helmholtz coil pair which surrounds a pipe completely filled with liquid metal. Between the emitter coils the resulting induction field is nearly compensated in absence of any fluid motion. As soon as flow occurs, the magnetic field lines are dragged downstream out of the compensated volume where a receiver coil L_R is placed. The flow induced phase-shift $\Delta\phi$ between the induced signal of the receiver coils is proportional to the magnetic Reynolds number. The flow rate sensor has to be calibrated as indicated by the factor K in Equation (5) in the same way as the lateral phase-shift sensor. The flow direction can be detected by the sign of the measured RMS signal from the receiver coil or the phase shift between the emitter and receiver coil.

2.2. Eddy current flow meter

The eddy current flow meter (ECFM) is based on the same principle as the phase shift sensor. The detector head consists of two detection coils L_R and one emitter coil L_E which is fed by an AC current. Contrary to the phase shift sensor, the ECFM can be placed inside a pipe or pool to detect the flow rate in a certain volume around the sensor. This volume is influenced by the frequency of the AC current and the electrical conductivity of the liquid metal. The information about the averaged velocity u_0 or flow rate Q can be obtained by measuring the voltage and/or

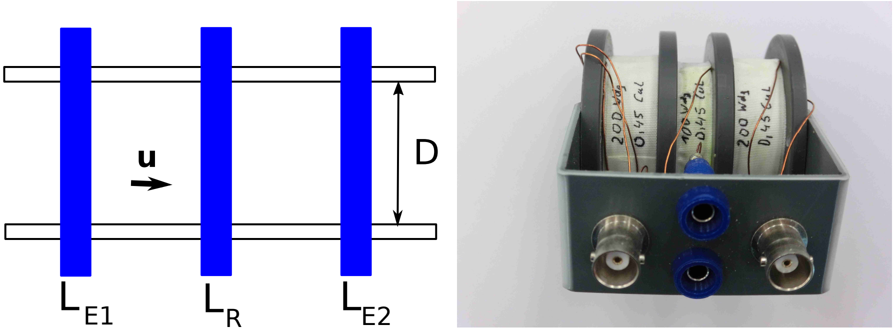

(a) (b)

Figure 4. Schematic diagram (a) and photo (b) of the axial phase-shift flowmeter with the emitting coils L_{E1} and L_{E2} and the receiving coil L_R around the pipe with diameter D.

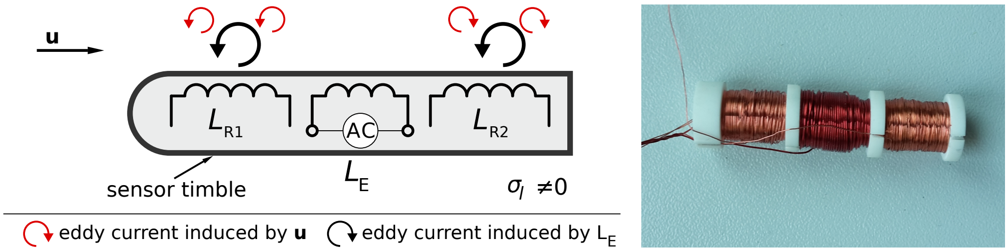

(a) (b)

Figure 5. Schematic diagram (a) and photo (b) of the eddy current flow meter with the emitting coil L_E and the receiving coils L_{R1} and L_{R2}.

phase difference between both detection coils, although the phase difference has proven to be more robust against outside disturbances. A stainless steel thimble protects the sensor coils from direct contact with the liquid metal.

Because of the transformer principle, L_E induces a certain voltage in both detection coils. This voltage is influenced by the presence of eddy currents within the medium around the sensor, which are also caused by L_E. There are two eddy current components, one is caused by the alternating electric field of L_E, the other is caused by the movement of the conductive medium through the magnetic field B of L_E. Because the radial component of B is opposite for L_{R1} and L_{R2}, the motion induced eddy currents also have opposite directions. Eventually this leads to different voltages in L_{R1} and L_{R2}. In Figure 5 the voltage in L_{R1} will decrease and the voltage in L_{R2} will increase with rising u_0. The results are similar to those shown in Figure 3, both voltage and phase difference have a linear dependency of u_0.

2.3. Transient eddy current flow metering

Most inductive flow meters have the disadvantage that the measured voltages depend not only on the flow rate but also on the electrical conductivity of the liquid metal or its temperature. Transient eddy current flow metering (TEC-FM) offers a way to strongly reduce the influence of electrical conductivity on the measurement results. This is achieved by creating a traceable eddy current system within the liquid metal and tracking its movement. In this section, two basic sensor arrangements, the external and immersed TEC-FM are described. Both sensors create the eddy current system by suddenly switching on or off a constant current and thus inducing eddy currents within the liquid metal, which are swept away with flow velocity in flow direction.

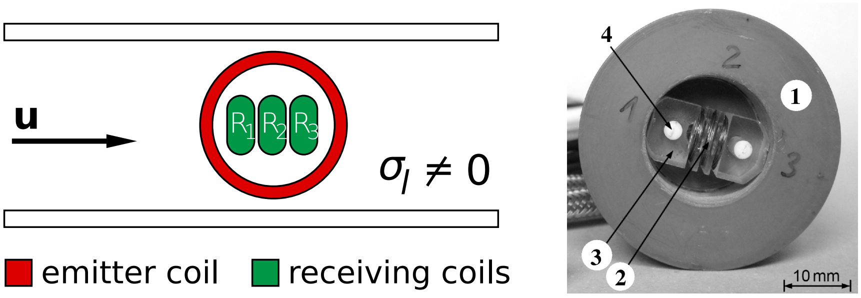

(a) (b)

Figure 6. Schematic diagram (a) and photo (b) of the external transient eddy current flow meter; emitter coil (1), three detection coils R_1, R_2 and R_3 (2), coil holder (3).

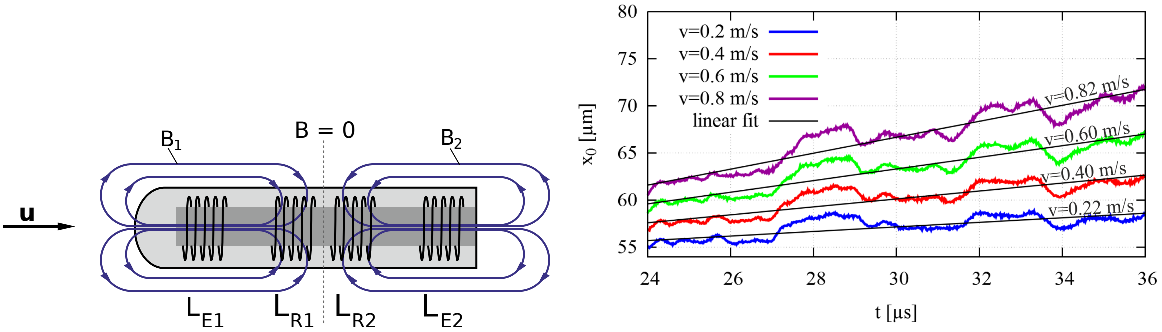

(a) (b)

Figure 7. Schematic diagram (a) with the emitting coils L_{E1} and L_{E2} and the receiving coils L_{R1} and L_{R2} and measurement results (b) for four different flow rates.

The external TEC-FM is placed outside of the boundary of the liquid metal, on a pipe for example. Figure 6 shows a schematic sketch and a photo of the TEC-FM sensor. The emitter coil of the external TEC-FM imprints an eddy current ring into the medium. The position of the magnetic pole x_{pp} of this ring is tracked by measuring and evaluating the voltages of the detection coils. The averaged flow velocity u_0 can be obtained by the time derivative of $x_{\mathrm{pp}}(t)$ [17].

Like the ECFM, the immersed TEC-FM is protected by a stainless steel thimble and can be placed inside a pipe or a pool to measure the local velocity in a certain volume around the sensor. It consists of two emitter and two detection coils. This technique tracks the position x_0 of the zero crossing of the magnetic field B of the imprinted eddy current system. The emitter coils L_{S1} and L_{S2} are fed by DC currents with equal magnitude but opposite directions. When the currents of both coils are switched on or off at exactly the same time, two oppositely directed eddy current rings are induced around the sensor with a magnetic flux density of zero in the middle between them (see Figure 7). This zero crossing is moving with u_0 and can be tracked by the detection coils. The measurement results are almost independent of the electrical conductivity of the liquid metal, so this technique can essentially be called calibration free [18].

When plotting the position of x_0 over time, the slope of the linear regression line of $x_0(t)$ indicates the average flow velocity u_0 around the sensor.

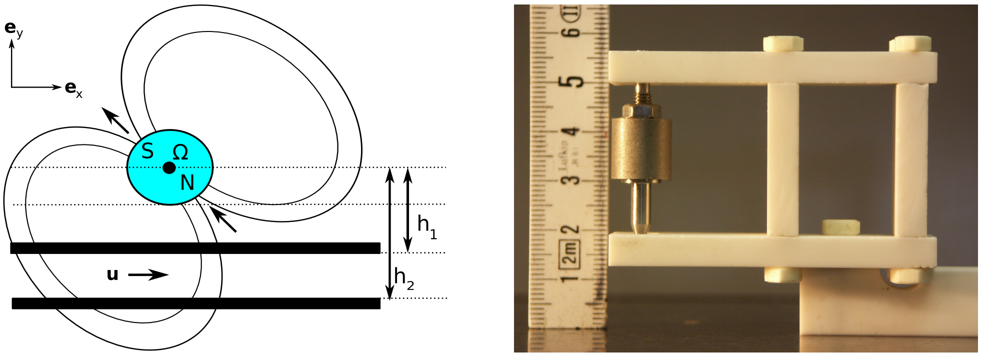

(a) (b)

Figure 8. Schematic diagram (a) and photo (b) of the rotary flow meter with the distances h_1 and h_2.

2.4. Rotary flow meter and magnetic flywheel

Contrary to the sensors presented previously, which used coils, the sensors described in the next sections employ permanent magnets. The rotary flow meter consists of a single cylindrical permanent magnet magnetized perpendicularly to its axis [19]. As shown in Figure 8(a) the sensor is placed close to the pipe and its axis is aligned perpendicular to the flow direction.

The theoretical analysis in [19] for the cases of a long as well as a short length of the cylindrical permanent magnet showed that its resulting equilibrium rotation does not depend on the strength of the magnet. It also does not depend on the conductivity of the liquid metal provided that the related skin-depth due to the rotation exceeds the distance h_2 as defined in Figure 8(a). In this case and, e. g., for a long magnet rotating steadily without a significant friction, the equilibrium rotation rate for a constant velocity u_0 in the channel is given by

$$\Omega = \frac{u_0}{2}\left(\frac{1}{h_1} - \frac{1}{h_2}\right) \ln^{-1}\left(\frac{h_2}{h_1}\right) . \tag{6}$$

A more complex permanent magnet flowrate sensor is the so-called magnetic flywheel as shown in Figure 9. Already in the sixties Shercliff [20] suggested such an electromagnetic flow meter consisting of a rotatable plate carrying a number of equidistantly spaced permanent magnets with alternating polarity. This solution was further developed [21] and received until today a number of applications at various liquid metal facilities.

2.5. Lorentz Force Velocimetry (LFV)

A typical LFV sensor consists of a pair of permanent magnets which embrace the pipe or channel containing the fluid [11, 22] as shown in Figure 10(a). Under the influence of the static magnetic field the flow generates a flow braking force (see Equation (4)) in the fluid. This force is proportional to the velocity or flow rate of the liquid and, due to Newton's third law, a force of the same magnitude but in opposite direction acts on the source of the applied magnetic field. The force $\vec{F}$ and torque $\vec{T}$ can be calculated by integrating $\vec{f}$ over the fluid domain using following integrals:

$$\vec{F} = \int_{Vol} \vec{j}(\vec{r}\,') \times \vec{B}_0(\vec{r}\,')\ dV' , \tag{7}$$

$$\vec{T} = \int_{Vol} (\vec{r} - \vec{r}\,') \times \vec{f}(\vec{r}\,')\ dV', \tag{8}$$

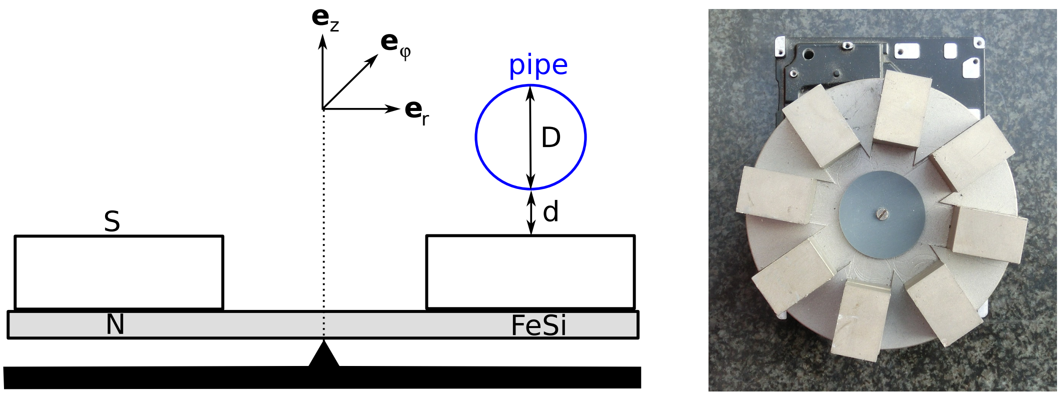

(a) (b)

Figure 9. Schematic diagram (a) and photo (b) of a flywheel flow meter.

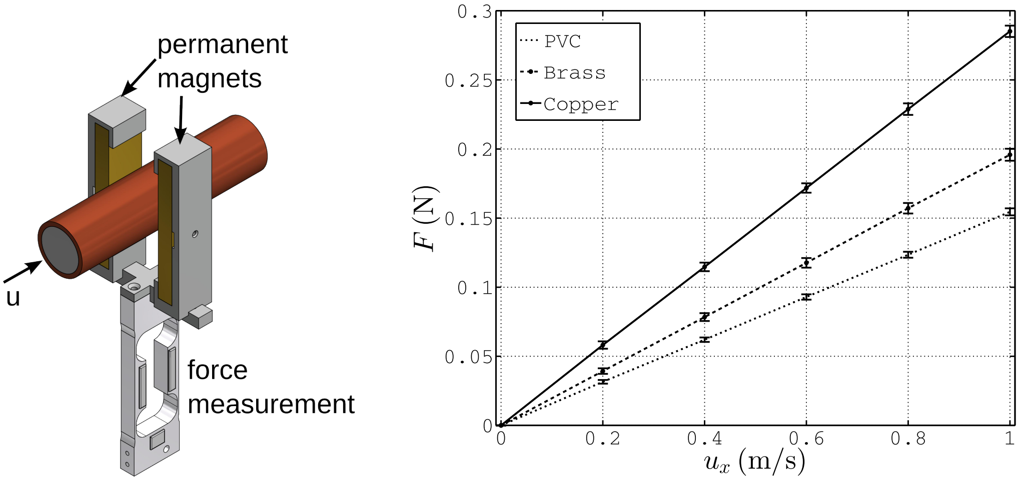

(a) (b)

Figure 10. Schematic sketch (a) of a LFV sensor and the measured force (b) for the three test sections made of PVC, brass and copper of the GaInSn loop shown in Figure 1.

respectively [23]. Here, dV' denotes the volume element, $\vec{r}\,'$ the position in the volume and $\vec{r}$ is the given reference point for the torque which could be either the center of the magnet or the center of the coordinate system which is defined by calibration.

Figure 10(b) shows a clear linear dependence between the measured force and the flow rate for the three different test sections made of PVC, brass and copper of the GaInSn loop shown in Figure 1. It is evident that in the case of conducting walls (brass and copper) the measured force increases depending on the electrical conductivity σ_w of the wall.

This effect was first addressed in the framework of Lorentz force velocimetry using a small-size magnet that was placed in front of the tubes [24]. Here, experiments and simulations showed that when the ratio between the conductivity of the wall σ_w and the liquid σ_l increased, $\vec{F}$ seems to rise asymptotically suggesting a limit of this effect. $\vec{F}$ is in this case the sum between $\vec{F_l}$ and $\vec{F_w}$ which are the Lorentz forces generated in the liquid and the wall, respectively.

In a new study, this effect is analysed in more detail by using an analytic and numerical model of the limiting case where the ratio of conductivities goes to infinity. Our results indicate that the total Lorentz force in the liquid $\vec{F_l}$ approaches asymptotically the Lorentz force term that depends on $\vec{u} \times \vec{B}_0$. The force component $F_{l,\phi}$ generated by the induced electric potential ϕ is sensitive to the ratio between conductivity of the wall and the liquid $\varepsilon_w = \sigma_w/\sigma_l$. Perfect conducting and perfect insulating behavior of the walls appear when $\log_{10}(\varepsilon_w) > 4.5$ and $\log_{10}(\varepsilon_w) < -4.5$, respectively. In the first case, $F_{l,\phi}$ is zero and in the second one it reaches its maximum value. In general, the force component generated by the induced potential is always opposite to that one given by $\vec{u} \times \vec{B}_0$. When $F_{l,\phi}$ is diminished by either increasing the electrical conductivity of the walls or by changing the aspect ratio of the flow, we can achieve a considerably increase of the measurable total Lorentz force, and therefore, enhance the sensitivity of the measurements. A publication explaining these effects in detail is in preparation.

3. Local Lorentz Force Velocimetry (local LFV)

By reducing the size of the permanent magnet used for LFV and owing to the rapid decay of magnetic fields, a localized magnetic field distribution in the liquid metal is achieved by using magnets which are significantly smaller compared to the cross-section of the flow. Hence, the measurable force is localized in a small subsection of the fluid giving access to a local velocity assessment. Due to its localized nature, the system composed of the small-sized magnet altogether with the force sensor is called Local Lorentz Force Flowmeter (L2F2). At the beginning of the project this concept of local LFV has already been experimentally tested by successfully identifying obstacles in the flow [13]. The first application of this measurement technique for the reconstruction of the two-dimensional velocity structure in the vicinity of the wall of a confined vessel [25] showed the applicability of this technique to complex flow structures. In these experiments, an one-dimensional Optical Interference Force Sensor (OIFS) was used [26]. This implies that for measuring the second component of the force, the sensor had to be rotated 90 degrees and placed again in the measuring grid introducing another source of error. In order to overcome these problems, the measuring device of the new generation L2F2 is a multicomponent force and torque sensor [27, 28]. This sensor has been specially developed to record simultaneously all three force and three torque components that act on the magnet. By using this sensor connected to a 15 mm cubic permanent magnet (CUBIC), we were able to assess the three-dimensional velocity of GaInSn near the wide face of the mold of a continuous casting model, the Mini-LIMMCAST facility (Liquid Metal Model for continuous casting of steel) [29]. A sketch of the set-up and the measurement grid is depicted in Figure 11(b). The double-roll structure, typical for continuous casting of steel, was clearly identified by both the force and torque signal. It turned out that the torque is less sensitive to ferromagnetic parts in the surrounding. The force F_z perpendicular to the wall showed the area where the liquid metal jet flowing out the SEN impinges onto the narrow faces of the mold. In this area the jet strongly diffuses and deviates in a upper and lower vortices. However, the torque component T_z co-aligned to this force was not accessible at all.

In order to optimize the magnet system to measure this torque, we have developed a numerical model of our experiments at the Mini-LIMMCAST facility in the framework of local LFV. Here, the magnetic Reynolds number Rm and the interaction parameter N are smaller than one. Thus, we are in the kinematic regime of LFV where the influence of the Lorentz force on the fluid is negligible [30]. Additionally, as the flow in the mold is steady, we can obtain the forces and torques directly from Ohm's law for a given velocity and applied magnetic field. This model was first verified with our experimental results with the CUBIC magnet and then used for optimization of the magnet system. Preliminary numerical and experimental results show that a cross-shape permanent magnet (CSM) (see Figure 11(c)) enhances considerably the torque perpendicular to the wall in comparison with the CUBIC magnet system. The torque T_z is expected to be in the order of 20 µN m at the Mini-LIMMCAST facility. Preliminary simulations suggest that this torque component correlates with the curl of the velocity in this direction. A publication giving more details about the simulation and the experiment with the CSM is in preparation.

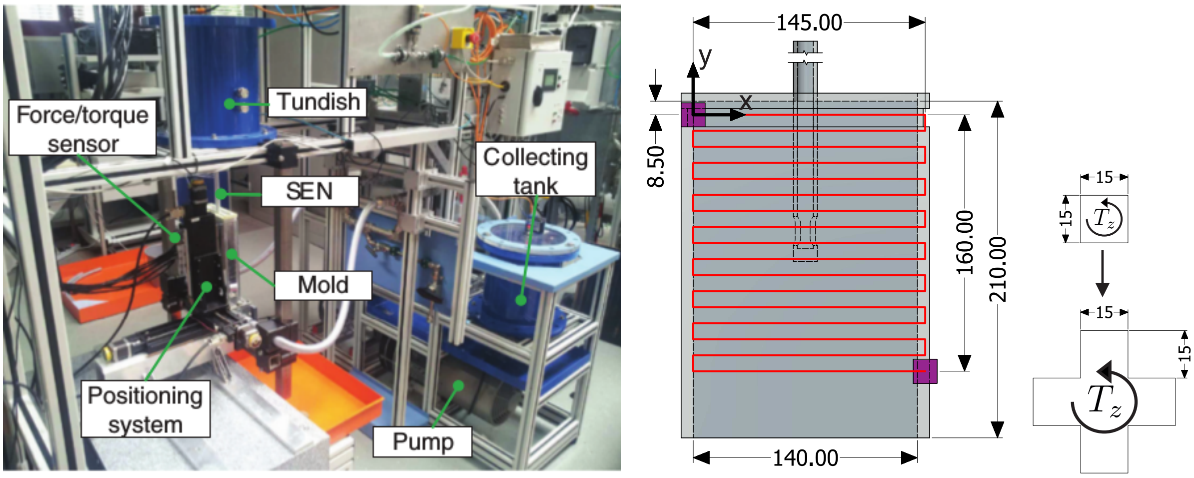

(a) (b) (c)

Figure 11. Picture of the Mini-LIMMCAST facility (a) with the force measurement system (see [29]), schematic sketch (b) of the mold presenting the measuring grid (red) and the location of the 15 mm cubic magnet (magenta) at the beginning ($x = 0$ mm, $y = 0$ mm) and at the end of the experiment ($x = 145$ mm, $y = -160$ mm), (c) schematic sketch of the CUBIC and the CSM magnets.

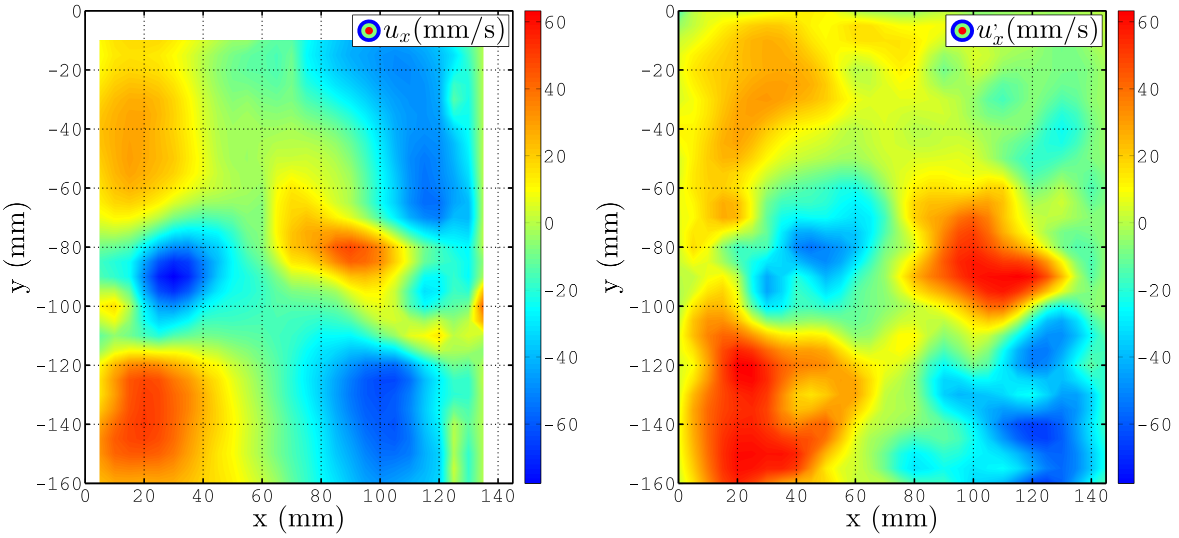

(a) (b)

Figure 12. Comparison between UDV measurement u_x near the wall *(a)* (taken from [29]) and the velocity component u'_x according to (9) using the measured force component acting on the magnet F_x *(b).*

Before using the CSM in liquid metal, we performed an electromagnetic dry calibration [31] of the L2F2 with a rotating disc made of aluminium. The advantage of this set-up is that we can accurately define the centroid of the magnet system for measuring T_z. This dry calibration technique can also be used to determine the calibration factor for the L2F2. The magnitude of the velocity field u' of the liquid metal is given by

$$u' = K_{liq} \cdot F \ , \tag{9}$$

where F is the magnitude of the measured force component and K_{liq} the calibration factor, respectively. However, one of the biggest challenges in local Lorentz force velocimetry is that K_{liq} does not only strongly depend on the distance between the permanent magnet and the liquid metal, but also on the velocity distribution near the wall spanned by the magnetic field.

In application, the velocity field in a given set-up is unknown and K_{liq} has to be defined *a priori* for a quantitative assessment of the velocity of the liquid metal next to the wall. This calibration factor can be estimated by the proposed dry calibration in the following way

$$K_{liq} = K_{disk} \frac{\sigma_{disk}}{\sigma_l} \ , \tag{10}$$

where K_{disk} and σ_{disk} are the calibration factor and conductivity of the disk, respectively. K_{disk} is the ratio between the velocity field in the disk and the force acting in the center of the magnet at (x_0, y_0). The position of the center of the magnet is sufficiently away from the rim of the disk in which the force is proportional to the radius r from the center of the disk. The CUBIC magnet system used in [29] is located at the same distance a_g away from the surface of the disk as in the experiments at the Mini-LIMMCAST facility. In this case, $K_{disk} = 2.7$ using a disk with 200 mm in diameter. Due to the comparably bigger distance and volume of the magnet system in comparison with the one used in [32], a bigger diameter of the disk has to be considered to avoid edge effects. Finally, the calibration factor in the Mini-LIMMCAST facility according to (10) is $K_{liq} \approx 2.7(25.4/3.3) = 20.8$. A comparison between the velocity field u_x measured by UDV [29] in comparison with the velocity field u'_x according to (9) is shown in Figure 12 having good agreement (rms(u_x)= 27.6 mm/s $\approx$ rms(u'_x)27.2 mm s^{-1}). With the proposed simple calibration procedure, we could obtain a conservative assessment of the magnitude of the velocity field at a depth of 4 mm at Mini-LIMMCAST facility. We believe that, in general, it can be used for a simple and fast approximation for K_{liq} regarding cubic or cross-shaped magnet systems. Further numerical investigation are currently being carried out out in order to define the penetration depth and spatial resolution of local LFV.

4. Contactless inductive flow tomography (CIFT)

In order to reconstruct the flow structure $\vec{u}$ from magnetic field measurements $\vec{b}$ outside the fluid volume V, Biot-Savart's law can be applied to Ohm's law (1) which leads to following integral equation:

$$\vec{b}(\vec{r}) = \frac{\mu_0 \sigma_l}{4\pi} \int\limits_V \frac{(\vec{u}(\vec{r}\,') \times \vec{B}_0(\vec{r}\,')) \times (\vec{r} - \vec{r}\,')}{|\vec{r} - \vec{r}\,'|^3} dV' - \frac{\mu_0 \sigma_l}{4\pi} \oint\limits_S \frac{\phi(\vec{s}\,')\vec{n}(\vec{s}\,') \times (\vec{r} - \vec{s}\,')}{|\vec{r} - \vec{s}\,'|^3} dS' \ . \tag{11}$$

In the volume integral, dV' denotes the volume element and $\vec{r}\,'$ the position vector in the volume. In the surface integral, dS' denotes a surface element and $\vec{n}(\vec{s}\,')$ denotes the normal vector of the surface S at the position $\vec{s}\,'$. The electrical potential ϕ at the boundaries is calculated by applying Green's theorem to the emerging Poisson equation (3) which leads to following integral equation

$$\phi(\vec{s}) = \frac{1}{2\pi} \int\limits_V \frac{(\vec{u}(\vec{r}\,') \times \vec{B}_0(\vec{r}\,')) \cdot (\vec{s} - \vec{r}\,')}{|\vec{s} - \vec{r}\,'|^3} dV' - \frac{1}{2\pi} \oint\limits_S \frac{\phi(\vec{s}\,')\vec{n}(\vec{s}\,') \cdot (\vec{s} - \vec{s}\,')}{|\vec{s} - \vec{s}\,'|^3} dS' \ , \tag{12}$$

if insulating boundaries are assumed. An extension of this integral system for conducting boundaries is given in [33]. In order to reconstruct the velocity field $\vec{u}$ in the volume V, this integral equation system has to be inverted. The intrinsic non-uniqueness problem of the emerging linear inverse problem, which mainly concerns the detailed depth-dependence of the velocity, is circumvented by utilizing the so-called Tikhonov regularization [12, 34].

The main challenge of CIFT is the reliable measurement of the induced magnetic field which is typically 2 to 5 orders smaller than the applied magnetic field. Therefore, a very stable current source for generating the excitation magnetic field and magnetic field sensors with a high dynamic range and a very linear response are needed. In order to make the measurement technique more robust against fluctuations of the environmental magnetic field, an AC excitation field with rather low frequency in the order of 1 Hz is used, such that the skin effect can be neglected. Using AC fields allows the actual induced magnetic field to be separated from the environmental noise suppressing undesired signals from the environment, like moving ferromagnetic materials, or arc welding activities in the vicinity of the experiment, because those are mainly DC signals [35, 33, 36].

At the beginning of the project a new measurement system consisting of 14 induction coils was designed and developed. The induction coils have two major advantages compared to Fluxgate sensors which were used previously: they can be applied in high temperature environments, and they can also work in the presence of strong static external magnetic fields. Induction coil sensors are only sensitive to magnetic fields which are variable in time, thereby suppressing static fields and significantly reducing the dynamic range of the measurement. Two different kind of coils are used: absolute and gradiometric induction coils. Absolute sensors consist of a single winding and detect the absolute value of the magnetic field, whereas gradiometric sensors comprise two windings, wound in opposing directions, which are connected in that way that a homogeneous external field is cancelled out. In order to detect the small flow induced magnetic fields, the absolute sensors have 340 000 turns and the gradiometric sensors have 2 × 160 000 turns. Both type of coils were made of 25 µm wire.

In order to test the robustness of the new sensor system, it was applied to the slab casting mold of the Mini-LIMMCAST facility in the presence of a strong static magnetic field generated by an electromagnetic brake (EMBr). EMBrs are widely used in continuous casting of steel to suppress flow fluctuations, which should lead to a more even solidification shell and less surface inclusions [38]. Figure 13 shows a schematic sketch and a photo of the Mini-LIMMCAST facility with the CIFT measurement equipment (excitation coil and pickup coils) and the EMBr. First experiments regarding CIFT and EMBrs were carried out with a preliminary setup, where just one excitation coil was used directly above the pole shoes of the EMBr, which resembles a previously used setup for the case without an EMBr [39, 40]. These preliminary measurements have delivered promising results, and demonstrated that the induced magnetic field (in the order of 100 nT) is indeed measurable on the background of a 310 mT field from the EMBr. The reconstructed velocity revealed that indeed an asymmetric flow structure was present when the EMBr is switched on while applying insulating boundary conditions [41], which is confirmed by UDV measurements [38].

The data gathered in these campaigns later served as a reference to gain further insight into the role of the significant eddy-currents in this setup by means of numerical simulations [37]. The strong eddy-currents appear even for very low frequencies $f < 10\,\mathrm{Hz}$ which are typical for CIFT.

The experimental setup was numerically modelled and could be accurately validated by the measurement data. Based on this model, forward (calculating $\vec{b}$ from $\vec{B}_0$ and $\vec{u}$) and inverse calculations (solving for $\vec{u}$) were carried out to systematically optimize the experimental setup.

The most relevant finding was that the excitation field from the high-positioned excitation coil is removed from the lower part of the mould by the pole shoes, which leads to âĂIJinvisibleâĂİ

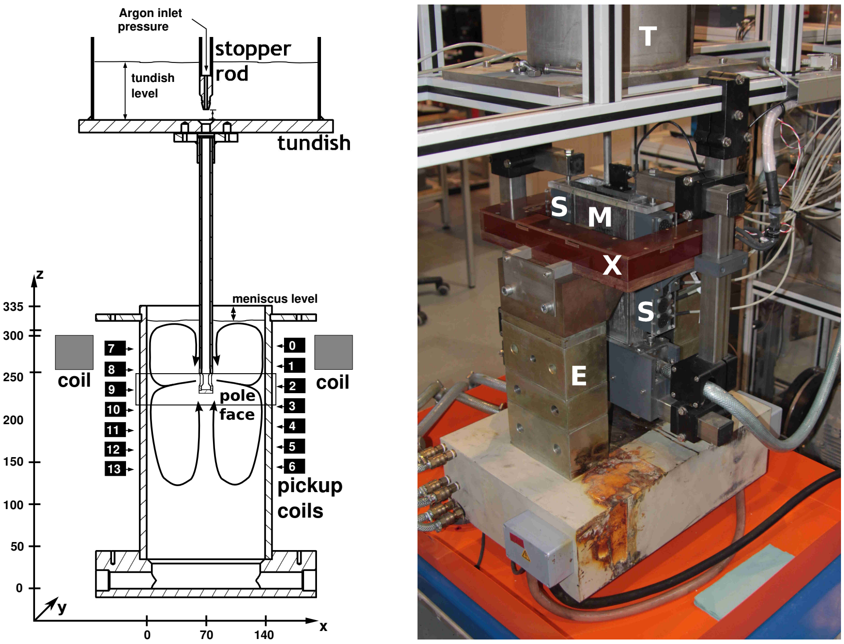

(a) (b)

Figure 13. Sketch and photo of Mini-LIMMCAST with the EMBr and the preliminary CIFT setup from [37]. E: EMBr, M: mould, S: sensors, T: tundish, X: excitation coil.

flow structures at the bottom of the mould. We concluded that a second excitation coil should be installed just below the pole shoes to accurately monitor the flow in this area.

The optimized setup was then installed and new experiments were carried out with low excitation frequency ($f \leq 3\,\mathrm{Hz}$), which matches the parameters of past experiments. Even though the three different cases (EMBr off, EMBr on with insulating or conducting boundaries) should all lead to vastly different magnetic field structures, the two cases with the EMBr turned on revealed the same magnetic field, which consisted completely of chaotic signals. Upon further investigation it could be demonstrated that low-frequency variations of the flow field together with the strong EMBr field generate a new magnetic field that is not related to the main flow structure (as desired by CIFT) but only to the flow variations, which then superimposes the CIFT induced field in a low frequency range [42]. The only possible solution in this case is the use of an excitation field in an higher and unaffected frequency range.

As soon as a higher excitation frequency (at least 8 Hz) is used, all three cases become distinguishable as can be seen in the plots in Figure 14. Unfortunately, the high frequency AC magnetic field generates eddy-currents that are so strong that the slight changes of the liquid metal level and the associated magnetic field in the mould would be visible on top of the flow induced field. This second effect that tends to superimpose our desired signal cannot be avoided and must therefore be compensated by means of calibration. Therefore, reference measurements were carried out where only the liquid metal level was changed without any liquid metal flow. The resulting magnetic field data can then be subtracted from real high-frequency flow measurements. It could be demonstrated that this method leads to accurate results [43].

However, due to the complex structure of the applied magnetic field, which is deformed by the ferromagnetic parts of the EMBr, and the recirculation flow close to the jets, the reconstruction of the flow was difficult to achieve with the present implementation of the forward model for CIFT. Therefore, new version of the forward model using linear and higher order elements is in development which allows the use of CIFT for arbitrary geometries. In order to investigate

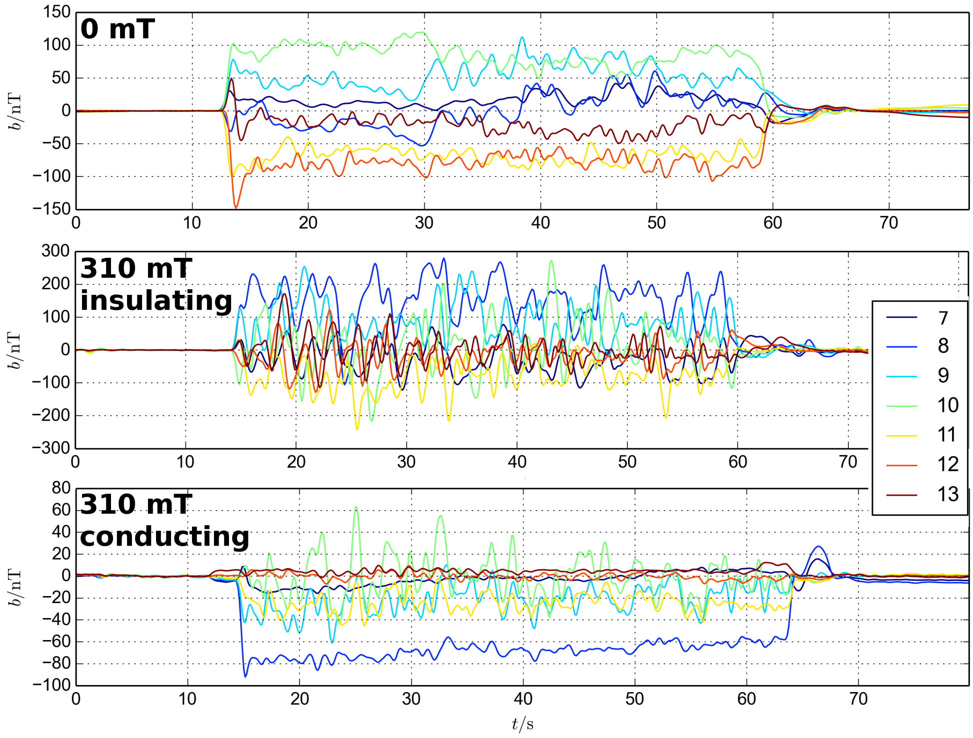

Figure 14. Comparison of the flow induced magnetic field measured by 7 gradiometric induction coils along the left side of the mold (see Figure 13) for the three cases EMBr switched off (a), EMBr switched on with insulating boundaries (b) and EMBr switched on with conducting boundaries (c), with an excitation frequency of 8 Hz.

thoroughly the accuracy of the new model, the calculation of the flow induced magnetic field for a rotating conducting cylinder in a homogeneous axial magnetic field is presently under investigation. In this configuration the flow induced magnetic field as well as the potential at the boundaries can be calculated analytically. Ongoing work is the test of this new model for the existing rectangular mold.

In order to investigate the scalability of CIFT to larger molds, a measurement system with 9 induction coils was developed and applied to the LIMMCAST facility which consists of a mold with the inner diameter of 0.4 m × 0.1 m [44]. The facility is operated with SnBi at 250 °C which poses new challenges to the instrumentation in terms of stiffness and temperature stability, and thereby resembles industrial facilities more closely.

Because of auxiliary equipment at the right side of the mould, sensors could only be installed at its left side. For the reconstruction, the measured magnetic field was mirrored to the right hand side. Figure 15 shows the magnetic field data and the reconstructed velocity for a typical experimental run with $f = 3\,\mathrm{Hz}$ and $I = 17\,\mathrm{A}$ [42]. Even though the conductivity of SnBi is about 0.4 of that of GaInSn and the distance between the sensors and the melt was increased to 10 cm, the sensors detect approximately the same magnetic field amplitude. It is evident that the flow in the mould is quite stable and just the overall intensity is subject to a small trend. The reconstruction clearly shows the jet leaving the SEN which hits the narrow wall at around $z = 1\,\mathrm{m}$ and then splits up to form the double-roll structure. This successful experiment demonstrates the scalability of CIFT.

A further challenge is the applicability of CIFT to low velocities in the order of $10\,\mathrm{mm\,s^{-1}}$. A first measurement setup for CIFT was developed and installed at a small thermally driven

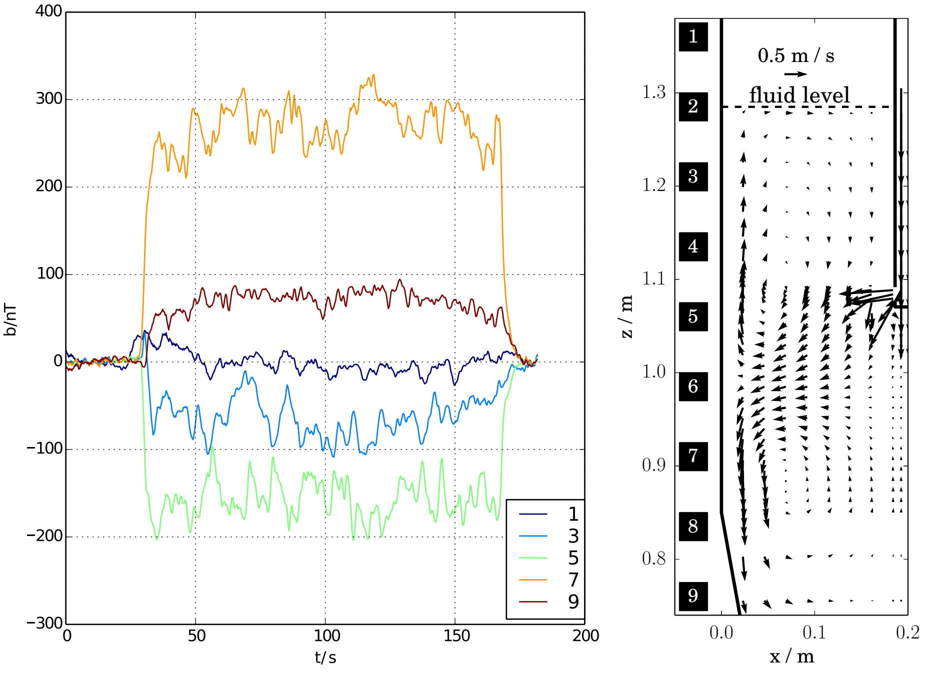

(a) (b)

Figure 15. Induced magnetic field (a) and reconstructed mean velocity (b) for a single run at LIMMCAST.

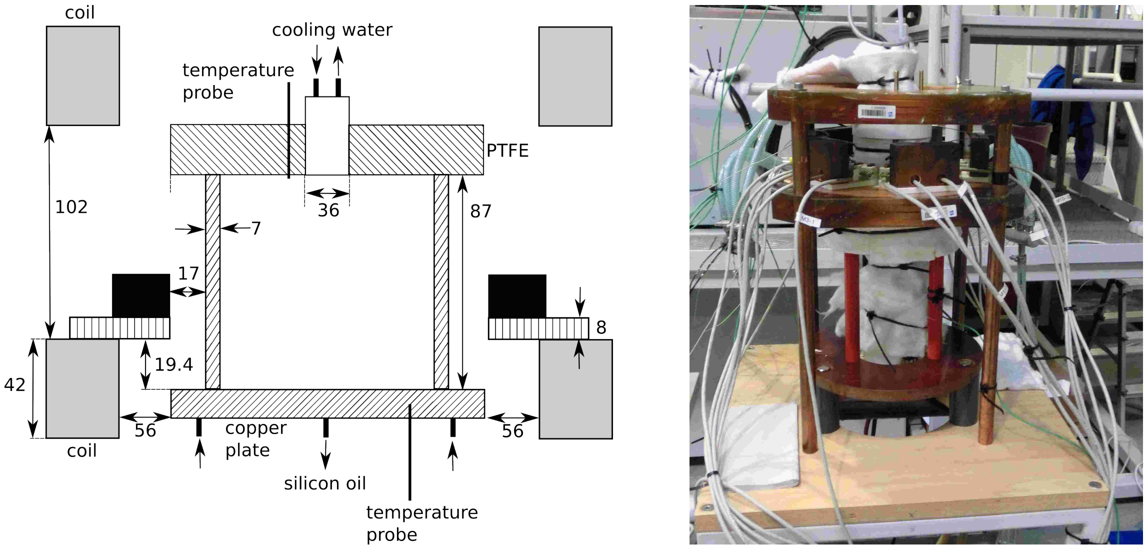

(a) (b)

Figure 16. Schematic sketch (a) and photo (b) of the modified Rayleigh-Bénard configuration.

flow experiment which is motivated by Czochralski crystal growth. In this case, the challenge is the robust detection of the weak flow induced magnetic field which is about 5 orders of magnitude smaller than the applied magnetic field [45]. In addition to the small velocities the long measurement time of more than 4 hours sets high demands on the stability of the measurement system. Due to these difficulties we started to develop the measurement system for one applied magnetic field while a full three-dimensional reconstruction is left for further investigations, which would require an additional applied magnetic field in horizontal direction.

Figure 16 shows a schematic sketch and a photograph of this setup, respectively. It consists of a cylindrical vessel filled with GaInSn, two coils which generate a vertical DC magnetic field of about 4 mT and 20 Fluxgate probes which are arranged over the azimuth at one height. This allows identifying the dynamics of the inclination angle of the large scale circulation (LSC) that is typical for this kind of flows. After removing all ferromagnetic parts and reducing the thermal expansion of the setup to a minimum, we were able to measure the magnetic field over 12 hours with a drift of about 20 nT during night.

Several experiments with temperature differences starting from $\Delta T = 2.3\,\mathrm{K}$ up to $\Delta T = 80.8\,\mathrm{K}$ were performed which showed a variety of flow phenomena. These include a LSC that is pinned at some angle from were it undergoes slight oscillations, and one cessation of the LSC. More details can be found in [45].

5. Ultrasound transit-time technique (UTTT)

Two general types of ultrasound methods have found their way into the research field of velocity measurements and two phase flows. One type of these techniques originates from non-destructive material testing techniques. These are the pulse-echo method and the transit time technique. The pulse-echo method evaluates the height of the echo amplitude and was already used by Matikainen et al. [46] to measure transient gas/liquid interfaces, and by Banerjee et al. [47] and Chang and Morala [48] to analyze single bubbles. The transit time technique focuses on the time of flight of the echo. In connection with advanced flow meters (Moore et al. [49], Mahadeva et al. [50]) the ultrasound transit time technique (UTTT) was developed. This technique is adequate to measure bubble parameters in liquid metal two-phase flows (Andruszkiewicz et al. [6], Richter et al. [51]). The other commonly used type of techniques is ultrasound Doppler velocimetry (UDV), which originates from medical application. UDV is a powerful technique to analyze flow structures (Takeda [52]) and was also successfully used to visualize wake structures of rising bubbles by Eckert et al. [5]. UDV and UTTT were already combined to study flow structures and bubble distribution of a bubble plume by Vogt et al. [53]. A recent technique for two-phase flows is the ultrasound reflector recognition and tracking technique (URRTT) which operates with pulsed ultrasound with the detection of the delay of the pulse reflection from a given bubble surface (Povolni et al. [54]).

The ultrasound transit-time technique (UTTT) operates with ultrasound transducers which emit acoustic pulses with a predefined frequency (in the range of MHz) and a given pulse repetition frequency $\mathrm{f_p}$ (in the range of kHz) through the wall of the vessel into the fluid. Figure 17(a) shows two transducers mounted at opposite sides of the wall of the vessel. The pulses are reflected by an object with a high acoustic impedance, which is either the opposing wall or the surface of the rising bubble, and detected by the emitting transducer. Suppose, the left transducer in Figure 17(a) emits one pulse, then Figure 17(b) shows the recorded amplitude of the echo for this configuration. The echo of both walls as well as of the left surface of the bubble is clearly visible. The time difference between emission and reception of the echos t_W (front wall), t_{BW} (back wall) and t_B (bubble) can be used to determine the distance of the objects, if the vessel diameter D is known.

The position x_B of the bubble surface next to the transducer can be calculated by [6]

$$x_B \;=\; D \cdot \frac{t_B - t_W}{t_{BW} - t_W}\;. \tag{13}$$

If two sensors i and j are mounted on opposite positions at the wall of the vessel, as shown

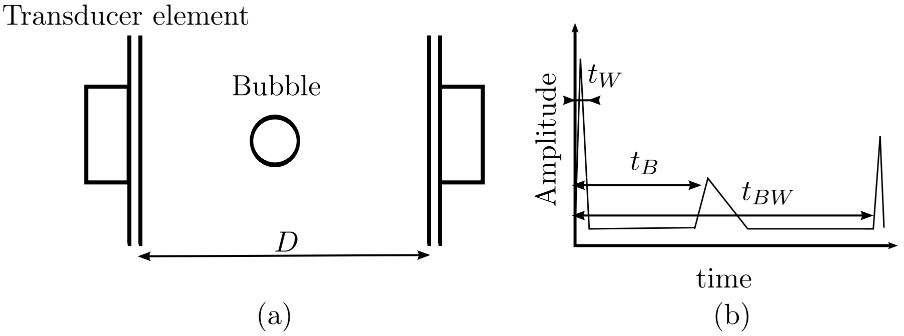

Figure 17. Schematic drawing illustrating all parameters necessary for the data extraction: the vessel cross section illustrating the diameter D (a) and the amplitude signal illustrating the transit times t_W, t_B and t_{BW} (b).

in Figure 17 (a), the diameter of the bubble is derived by

$$d_B \;=\; D \cdot \left(1 - \frac{t_{Bi} - t_{Wi}}{t_{BWi} - t_{Wi}} - \frac{t_{Bj} - t_{Wj}}{t_{BWj} - t_{Wj}}\right) \; . \tag{14}$$

It is obvious that the measured bubble surface shows fluctuations due to the entry and the exit of the bubble into the ultrasound beam. The center of mass x_{Bc} of the bubble is given by

$$x_{Bc} \;=\; x_B + \frac{d_B}{2} \; . \tag{15}$$

By using a test with falling steel balls the error of the method could be calculated to 7 % [55].

In order to measure the motion and trajectory of a bubble in the fluid volume, a combination of several sensors is used. Figure 18(b) shows a typical sensor arrangement. The transducer array is connected to a ultrasonic defectoscope (USIP 40 GE Inspections Technologies GmbH) which has 10 channels. This offers the possibility either to measure with 10 transducer elements, regardless to the number of arrays, to cover bubble trajectories, or to work with 5 pairs of opposing transducer elements to measure the bubble diameters and the trajectory during the rise [6].

While in previous work only the spatial distribution of bubbles was investigated, in the beginning of the project the tracking of single bubbles was implemented. This required a detailed analysis of the accuracy of the measurement. Therefore, the rise of a single argon bubble in water was simultaneously covered by UTTT and a high-speed camera. The intention of these measurements was to provide a deeper understanding of the measured diameter depending on the shape and the motion of the bubble. Figure 19(a) shows the measured trajectory with two pictures of the high-speed camera visualizing the bubble and Figure 19(b) shows the bubble diameters for the same height. The strong variation of the measured bubble diameters is caused by the tilting of the bubble, and thus UTTT measures a smaller apparent bubble diameter [55].

For an exact determination of the bubble diameter, the pair of ultrasound transducers on opposite sides have to be accurately aligned along their axis. As Figure 18(a) shows, there was a slight deviation of the sensor alignment between opposite sensors of the two arrays. Therefore, two new sensor arrays made out of one slide of piezoceramics were build. Each sensor consists of 32 elements with the dimensions 2.5 mm × 5.0 mm. In this case a better alignment of the sensors could be achieved. The high number of transducers allows a much more flexible adjustment of the distance between the single sensors to cover the bubble trajectory. Furthermore two transducer elements can be combined to one excitation element which increases the measurement plane.

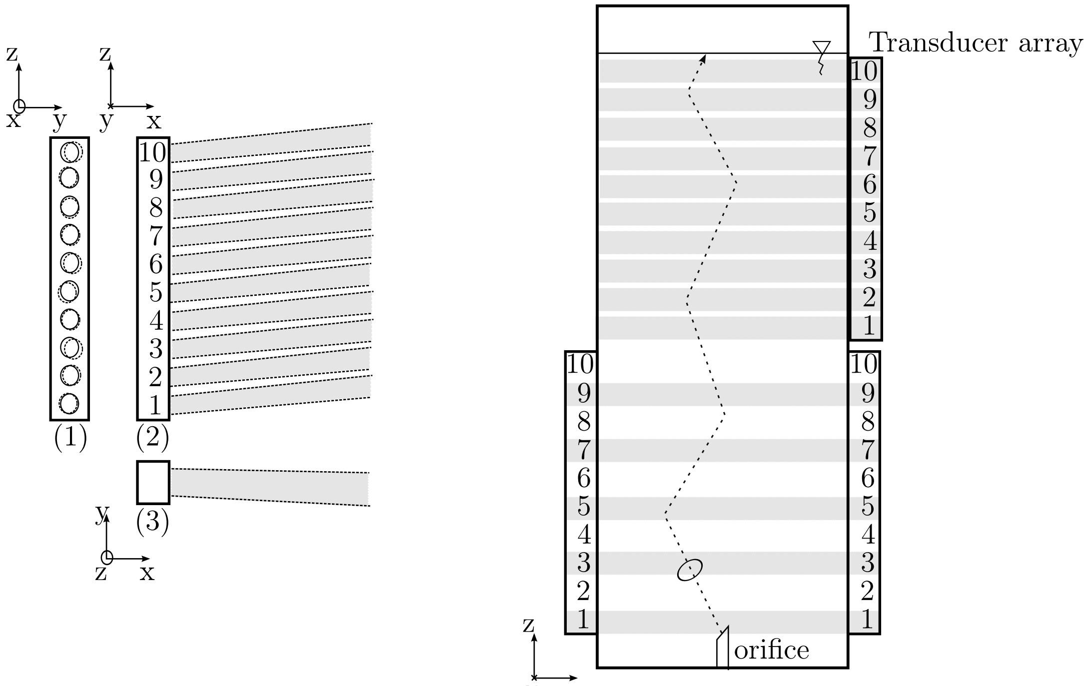

(a) (b)

Figure 18. Schematic drawing illustrating a transducer array with 10 elements (a). The dotted lines display the deviation of the actual positions with respect to the nominal ones (Sketch 1). Sketches 2 and 3 visualize the deviation in the alignment of the ultrasonic cones from side and top. Visualization of different combinations of transducer elements (b), above usage of 10 single transducer elements to cover bubble trajectories, below combination of 5 pairs of opposing transducer elements to cover the bubble diameters.

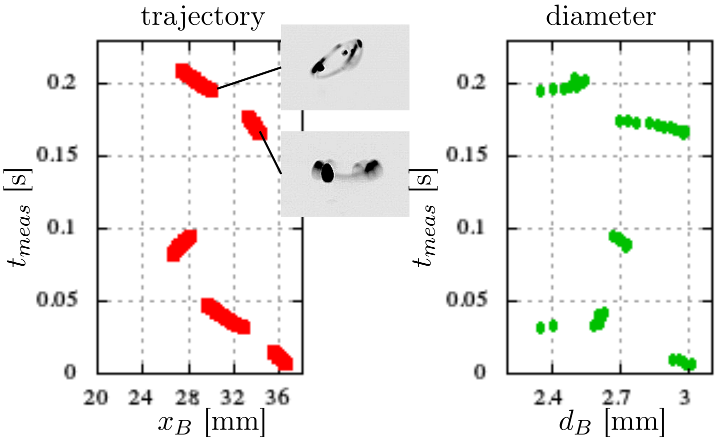

(a) (b)

Figure 19. Bubble trajectory with pictures of the high-speed camera (a), bubble diameters of a single bubble rising in water (b).

The measurements of the rise of single argon bubbles in GaInSn with an applied static horizontal magnetic field underlined the suitability of UTTT for the detection of the bubble diameter in liquid metal two-phase flows [51]. Exemplary, Figure 20 presents the trajectory

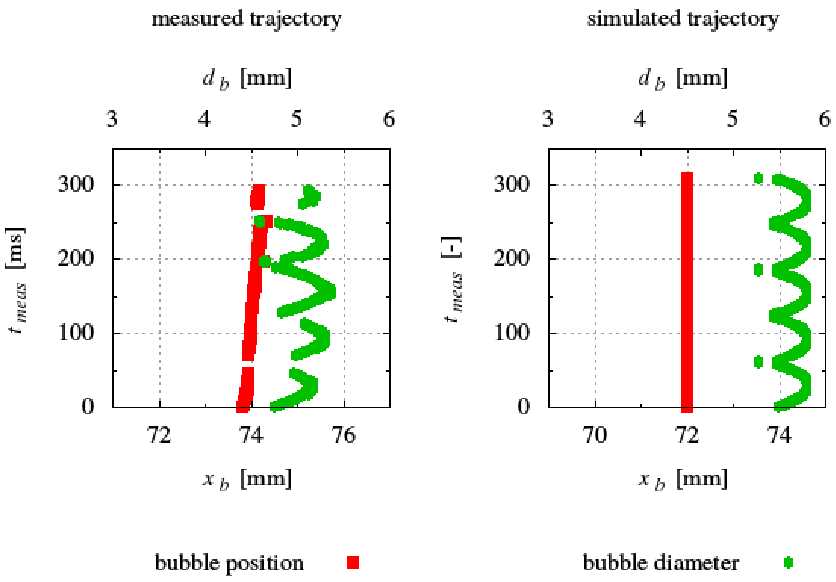

Figure 20. Comparison of measured and simulated bubble trajectory and diameter curves of a bubble rising in GaInSn.

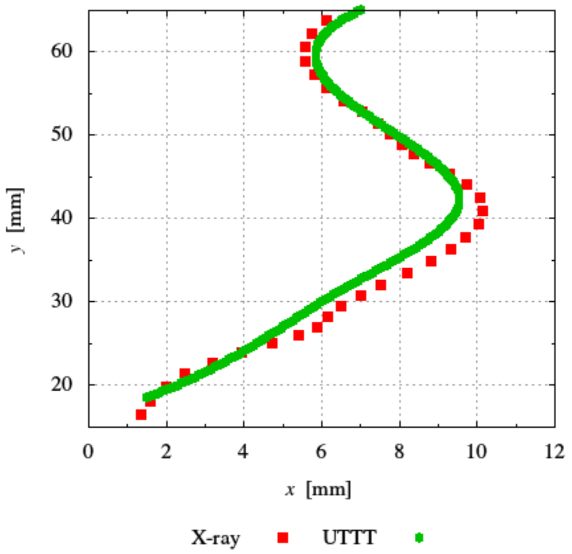

Figure 21. Comparison of bubble trajectories measured by UTTT and X-ray radiography.

and diameter of one argon bubble rising in GaInSn under the influence of a static horizontal magnetic field. As expected, the bubble rises on a nearly straight path. In order to get a better understanding how the shape and the position of the bubble effect the measurement, a ray tracing algorithm was developed which models the ultrasonic beam as a bundle of rays, which are partly reflected by the bubble modelled as an ellipsoid. With this method the trajectory and the diameter of the bubbles were simulated and compared in Figure 20 with the experimental results. A good agreement could be observed.

In order to validate the measurements of UTTT in GaInSn, the trajectory and size of the rising bubbles without an applied magnetic field were recorded by the means of X-ray radioscopy. Figure 21 displays the trajectory of one rising bubble measured by the means of UTTT and X-ray radiography. Again, a good agreement could be achieved.

For the measurement of bubble chains and bubble swarms, the sensor arrays are aligned horizontally. This enables a complete scanning of the cross section of the fluid container for the detection of the position and the diameter of rising bubbles. If two transducer arrays are positioned at two different heights, the rising velocity can also be estimated. Furthermore, the new setup offers the possibility to use UTTT as a void fraction measurement method.

Preliminary measurements at the Mini-LIMMCAST facility suggest that UTTT may be able to get information about the bubble injection through the SEN and the movement of the bubbles in the mold.

6. Inductive bubble detection

Inductive bubble detection methods typically apply a time varying magnetic field to the melt. The induced eddy currents are deformed when a bubble moves through the melt, because the bubbles are electrically insulating. The governing equation is following differential equation

$$\nabla^2 \vec{A} = \mu_0 \sigma \frac{\partial \vec{A}}{\partial t} \tag{16}$$

with the vector potential $\vec{A}$ and the spatially varying electrical conductivity σ in the volume. The eddy currents in the melt generate a secondary magnetic field which perturbs the applied magnetic field and depends on the spatial variation of σ. This secondary magnetic field can be measured outside the melt and depends on the geometry of the conducting volume.

One promising technique is MIT which allows the reconstruction of the conductivity distribution in one cross section of a pipe [9]. In general, N coils are equally spaced around the imaging area which results in $N(N-1)/2$ independent measurements of the mutual inductances between the coils. In order to reconstruct the conductivity distribution, Equation (16) has to be inverted. This leads to a non-linear inverse problem which is difficult to solve.

A sensor using eight coils was already used to visualise the position of the liquid metal strand in the SEN in a real caster [9] and in a cold model [56, 40]. The outer surface of the liquid metal jet in the SEN could be reliably reconstructed. However, bubbles inside the liquid could not be identified. Due to the non-linear inverse problem which has to be solved for MIT it is evidently very difficult to reconstruct the surface of the liquid metal column and the bubbles in the melt at the same time. One solution could be the combination of MIT for visualizing the interior of the liquid metal with the electrical capacitance tomography (ECT) for visualizing the outer shape of the liquid metal strand. In a first feasibility study it could be shown that ECT is able to detect the outer surface of liquid metal [57].

In applications like the stagnant bubble reactor for methane pyrolysis the interesting parameters are the trajectory and the size of the bubbles. The high temperature over 800 °C and the high corrosiveness of liquid tin prevent the use of ultrasonic or invasive measurement techniques. Up to now, no appropriate sensor is available. In order to reduce the complexity of the MIT system for detecting bubbles in a pipe filled with liquid metal, a new sensor consisting only of one excitation coil and one planar gradiometer coil on opposite sides of the pipe was developed [58]. The intention of this sensor was the detection of bubbles which are traversing the sensitive region of the sensor without solving any inverse problem. The sensor was tested in GaInSn and in sodium. Numerical simulation suggested that the recorded signal contains information about the position and the size of the bubble, but it is evidently difficult to extract

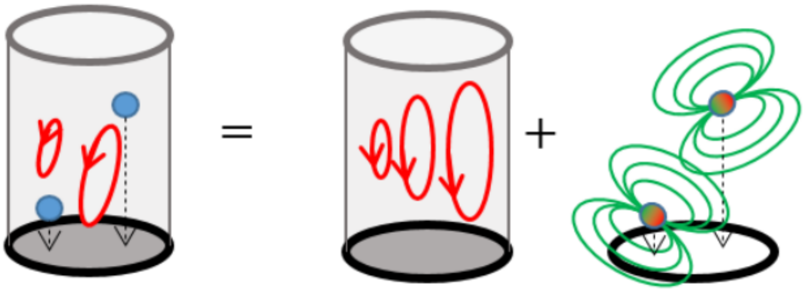

Figure 22. Principle of the dipole: instead of calculating the whole current-distribution for a changed geometry, the field of a reference case is corrected with the dipole fields substituting the bubbles.

this information from one single measured voltage of the detection coil. As a consequence, the inversion is ambiguous. This problem can be overcome by using an array of excitation and detection coils to reconstruct the bubble distribution from different positions.

Instead of recalculating the current distribution in the observed volume for every bubble distribution, only the reference case without any bubble is calculated. If a comparably small bubble is placed in the observed volume, the main difference in the current distribution is the absence of electric currents in the bubble volume. As simplification, the change of the secondary magnetic field is modelled by an appropriate magnetic dipole which compensates the magnetic field from the reference case as seen in Figure 22. In the case of a spherical bubble in a sinusoidal excitation field, the equation for the momentum is given by

$$m_{dipole}(t) = -\frac{8\mu_0\pi\sigma_l\omega B_0}{15} \cdot R^5_{bubble} \cdot cos(\omega t) \ , \tag{17}$$

where R_{bubble} is the radius of the sphere and B_0 is the amplitude of the excitation field at the center of the bubble.

This model has some significant advantages as the dipole has a directed field and scales linearly with the number of bubbles. For the reconstruction of the bubble distribution a distribution of dipoles has to be found which corresponds to the detected signal. The measured magnetic field H_{total} at the detection coils can be written as following sum:

$$H_{total} = H_{excitation} + H_{reactor} - \sum H_{dipoles} \ . \tag{18}$$

$H_{excitation}$ is the magnetic field of the excitation coil, $H_{reactor}$ is the field generated by the eddy currents and H_{dipol} are the fields of the magnetic dipoles substituting the bubbles.

For a reliable measurement of the magnetic field of the dipole, gradiometric detection coils are used and the excitation and detection coils are placed in a special arrangement so that the magnetic field from the excitation coil is nearly eliminated at the detecting coils. In this case, only the magnetic field of the dipoles is measured.

Figure 23 shows a schematic sketch and a photo of the first experimental setup. The entire sensor consists of two planes with three coils each. Each coil consists of an excitation (red) and receiving (green) coil. For each plane three differential measurements from three perspectives can be obtained. This allows the detection of single bubbles in the cross section of the volume. The two planes are used to detect the movement of the bubble in vertical direction. The first experiment at room temperature is set up in order to test the new sensor. A non-conductive phantom of a bubble at the tip of a metallic rod can be inserted from above at any place inside the vessel. Objectives are the optimal positioning of the coils and the analysis of bubble swarms.

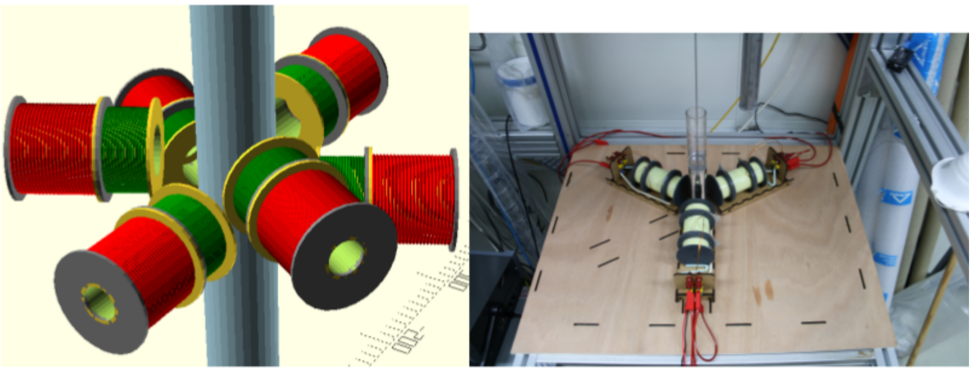

Figure 23. Schematic sketch of the sensor and a picture of the experimental setup using only three coils.

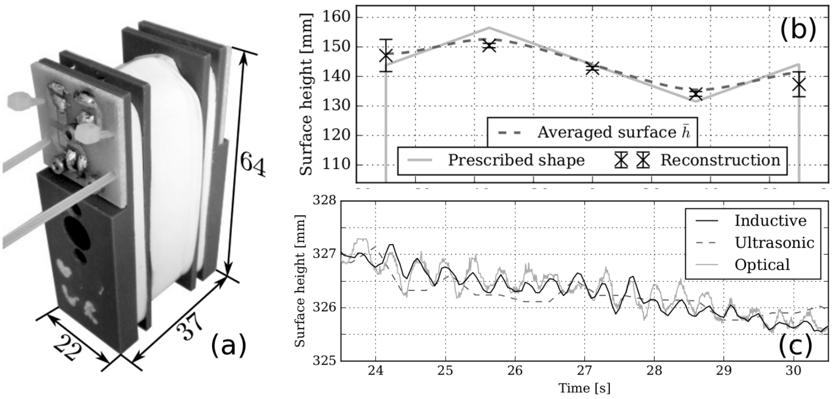

Figure 24. Inductive sensor (a) with dimensions in mm; test measurement (b) at a container with a zig-zag surface; experimental validation (c) in comparison to other measurement techniques [59].

The challenge to adapt the new sensing system to the high temperature are left for further investigations. Among them are the construction of high temperature coils, thermal shielding as well as filtering out the electromagnetic field generated by the heaters.

7. Inductive level measurement sensor

One industrial problem is the accurate and fast determination of the melt level in various processes incorporating molten metals or semiconductors. For this we developed a sensor which consists of an oval shaped excitation coil at the center of the body and two oval shaped receiver coils connected to form a gradiometric coil, positioned symmetrically from the center coil (Figure 24(a)). The sensor permeates the melt with an AC magnetic field, which generates eddy-currents, that in turn give rise to a secondary magnetic field. The primary field is suppressed by the gradiometric receiving coils, which results in a good signal-to-background ratio for the secondary field. The conversion from magnetic field amplitude to liquid level is carried out by calibration and subsequently fitting a sigmoid function to the data [59].

In order to evaluate the sensor we performed static and dynamic tests. The static test consisted of a liquid metal container with the dimensions of the Mini-LIMMCAST slab mould, filled with GaInSn and a zig-zagged PVC block on top of the liquid, which creates a non-flat surface shape which can be measured by the sensor. We positioned the sensor successively at five evenly distributed horizontal positions along the wide face of the container and reconstructed the level at this position (Figure 24(b)). While the extrema are underestimated because of the nature of the eddy-currents which occupy the whole available volume, the measured levels are very close to the calculated averaged surface.

The dynamic test was conducted at Mini-LIMMCAST itself and evaluates the sensor performance in comparison to an ultrasonic sensor (sampling frequency 2.8 Hz) and a laser scanner (93 Hz), as seen in Figure 24(c). During Mini-LIMMCAST operation surface waves are propagating between the two narrow faces, resulting in a seesaw motion of the surface. While the ultrasonic sensor has a too low sampling frequency to detect the surface waves at Mini-LIMMCAST, the optical and our inductive sensor show a striking similarity, thereby suggesting a sub-millimeter resolution of our sensor at a time-resolution of 20 Hz until now. A patent application has been filed and is under review.

8. Conclusion

In this short review, the recent developments of flow measurement techniques in the framework of the Helmholtz Alliance LIMTECH were presented. At the beginning, an overview of different inductive flow rate sensors for ducts and pipes were given. These techniques include TEC-FM, which is calibration free, and LFV, which was tested with different wall conductivities. The extension of LFV, which is called local LFV, allows the investigation of flow structures close to the wall. It was applied for the first time to a complex flow in a cylindrical vessel and to the flow structure at the wide face of a slab casting mold. A new three dimensional sensor is capable of measuring all three force and torque components at the same time. By applying a dry calibration of the new sensor, the velocity distribution along the narrow face could be calculated and compared to UDV measurements.

A different flow measurement technique is CIFT which allows the reconstruction of the mean three-dimensional velocity structure in liquid metals. By using gradiometric induction coils for the magnetic field measurement in combination with an AC excitation magnetic field with low frequency, the magnetic field measurements are less sensitive to fluctuations of the environmental magnetic field. This was demonstrated by the reliable measurement of the small induced magnetic field along the narrow faces of the wall of a slab casting mold even in the presence of a strong static magnetic field generated by an electromagnetic brake. Additionally it could be shown that the dynamics of a typical large scale circulation in a temperature driven experimental setup can be reconstructed. The challenge in this case is the magnitude of the velocity which is one order of magnitude smaller than in the case of continuous casting.

For the measurement of two phase flows in large vessels, UTTT can be used which allows the measurement of trajectories and diameters of bubbles. In order to understand the dependence between the shape of the bubble and the diameters measured by UTTT, experiments in water as well as in GaInSn were conducted. These measurements were compared with optical and X-ray measurements. Additionally, a simulation of the ultrasound beam based on ray tracing was developed. These developments provide a sound basis for the investigations of complex two-phase flow regimes like in a continuous casting mold.

In order to investigate bubble behavior in high temperature melts, a quite new inductive method based on MIT is under development. While for MIT a non-linear inverse problem has to be solved in order to reconstruct bubbles, the new sensor system will use a different strategy, by modelling the bubbles as a single magnetic dipole which perturb the applied magnetic field.

While the LIMTECH Alliance is about to end, the developed techniques are taken to the next step of industrial application with experienced industrial partners. This includes a collaboration with SolarWorld Innovation GmbH in Freiberg regarding Czochralski crystal growth and with an manufacturer of continuous steel casting plants. Additionally, an innovative training network called TOMOCON will start in summer 2017. The aim of this project is the integration of tomographic sensors into process control. One of the four planned demonstrators will be the control of continuous casting using CIFT and MIT.

List of acronyms

CIFT	contactless inductive flow tomography
CSM	cross-shape magnet
ECFM	eddy current flow meter
ECT	electrical capacitance tomography
EMBr	electromagnetic brake
GaInSn	gallium-indium-tin
L2F2	local Lorentz force flowmeter
LFV	Lorentz force velocimetry
LIMMCAST	liquid metal model of continuous casting
LIMTECH	liquid metal technologies
LSC	large scale circulation
MIT	mutual inductance tomography
SEN	submerged entry nozzle
SnBi	tin-bismuth
TEC-FM	transient eddy current flow meter
UDV	ultrasound Doppler velocimetry
UTTT	ultrasound transit-time technique

Acknowledgments

Financial support of this research by the German Helmholtz Association in the frame of the Helmholtz-Alliance LIMTECH is gratefully acknowledged. The authors are also grateful to Deutsche Forschungsgemeinschaft (DFG) for the financial support in the framework of Research Training Group Lorentz Force Velocimetry and Lorentz Force Eddy Current Testing (GRK 1567) at Technische Universität Ilmenau. We thank Shenyi Qin, Till Zürner and Robert Martin for their valuable contributions to CIFT, as well as Frank Stefani and Sven Eckert for fruitful discussions, and Klaus Timmel for technical support.

References

[1] Manning C P and Fruehan R J 2001 *JOM* **53** 34–43
[2] Zhang L and Thomas B 2003 *ISIJ International* **43** 271–291
[3] Seerban M, Lewis M, Marshall C and Doctor R 2003 *Energy Fuels* **17** 705–713
[4] Yasushi Takeda 1987 *Nuclear Technology* **79** 120–124
[5] Eckert S, Gerbeth G and Melnikov V I 2003 *Experiments in Fluids* **35** 381–388 ISSN 0723-4864
[6] Andruszkiewicz A, Eckert K, Eckert S and Odenbach S 2013 *The European Physical Journal Special Topics* **220** 53–62
[7] Saito Y, Shen X, Mishima K and Matsubayashi M 2009 *Nuclear Instruments and Methods in Physics Research Section A: Accelerators, Spectrometers, Detectors and Associated Equipment* **605** 192 – 196
[8] Timmel K, Shevchenko N, Röder M, Anderhuber M, Gardin P, Eckert S and Gerbeth G 2015 *Metallurgical and Materials Transactions B* **46** 700–710
[9] Ma X, Peyton A, Binns R and Higson S 2005 *IEEE Sensors Journal* **5** 224–232
[10] Priede J, Buchenau D and Gerbeth G 2011 *Measurement Science and Technology* **22** 055402
[11] Thess A, Votyakov E V and Kolesnikov Y 2006 *Physical Review Letters* **96** 164501 ISSN 0031-9007
[12] Stefani F, Gundrum T and Gerbeth G 2004 *Physical Review E* **70** 056306 ISSN 1539-3755
[13] Heinicke C 2013 *Experiments in Fluids* **54** ISSN 0723-4864
[14] OECD Nuclear Energy Agency 2015 *Handbook on Lead-bismuth Eutectic Alloy and Lead Properties, Materials Compatibility, Thermal-hydraulics and Technologies* 2nd ed (OECD)
[15] Buchenau D, Eckert S, Gerbeth G, Stieglitz R and Dierckx M 2011 *Journal of Nuclear Materials* **415** 396–403
[16] Schulenberg T and Stieglitz R 2010 *Nuclear Engineering and Design* **240** 2077–2087
[17] Forbriger J and Stefani F 2015 *Measurement Science and Technology* **26** 105303

[18] Krauter N and Stefani F 2017 *Measurement Science and Technology* ArXiv: 1703.09116
[19] Priede J, Buchenau D and Gerbeth G 2011 *Journal of Applied Physics* **110** 034512
[20] Shercliff J A *The Theory of Electromagnetic Flow-Measurement* (Cambridge Science Classics) ISBN 978-0-521-33554-6
[21] Bucenieks I 2002 *Proceedings of the 5th PAMIR Int. Conference, Sept. 16-0, Ramatuelle, France* pp II–103
[22] Thess A, Votyakov E, Knaepen B and Zikanov O 2007 *New Journal of Physics* **9** 299 ISSN 1367-2630
[23] Thess A and Böck T 2013 *IEEE Transactions on Magnetics* **49** 2847–2857 ISSN 0018-9464
[24] Kazak O, Heinicke C, Wondrak T and Böck T 2015 *Magnetohydrodynamics* **51** 579–588
[25] Heinicke C and Wondrak T 2014 *Measurement Science and Technology* **25** 055302 ISSN 0957-0233
[26] Füßl R and Jäger G 2009 *Fundamental and applied metrology: IMEKO XIX world congress, September 6 - 11, 2009, Lisbon, Portugal* (Budapest: IMEKO) pp 235–238 ISBN 978-963-88410-0-1
[27] Schleichert J, Rahneberg I and Fröhlich T 2013 *International Journal of Modern Physics: Conference Series* **24** 1360017
[28] Schleichert J, Rahneberg I, Marangoni R R and Fröhlich T 2016 *tm - Technisches Messen* **83** ISSN 0171-8096
[29] Hernández D, Schleichert J, Karcher C, Fröhlich T, Wondrak T and Timmel K 2016 *Measurement Science and Technology* **27** 065302
[30] Heinicke C, Tympel S, Pulugundla G, Rahneberg I, Böck T and Thess A 2012 *Journal of Applied Physics* **112** 124914
[31] Hernández D, Karcher C and Wondrak T 2016 *Proceedings of the 10th PAMIR International Conference, June 20-24, 2016, Cagliari, Italy* (Cagliari: PAMIR Centre) pp 198–202 ISBN 978-88-905519-3-2
[32] Hernández D, Böck T, Karcher C and Wondrak T 2017 *Magnetohydrodynamics* **53** 3–13
[33] Ratajczak M, Wondrak T, Zürner T and Stefani F 2015 *2015 IEEE Sensors* 7370342
[34] Stefani F and Gerbeth G 2000 *Inverse Problems* **16** 1–9
[35] Wondrak T, Eckert S, Gerbeth G, Stefani F, Timmel K, Peyton A, Terzija N and Yin W 2014 *Steel Research International* **85** 1266–1273
[36] Wondrak T, Ratajczak M, Gundrum T, Stefani F, Krauthäuser H G and Jacobs R T 2015 *2015 IEEE International Symposium on Electromagnetic Compatibility* 306–311
[37] Ratajczak M, Wondrak T, Stefani F and Eckert S 2015 *Magnetohydrodynamics* **51** 461–471
[38] Timmel K, Eckert S and Gerbeth G 2011 *Metallurgical and Materials Transactions B* **42** 68–80
[39] Wondrak T, Galindo V, Gerbeth G, Gundrum T, Stefani F and Timmel K 2010 *Measurement Science and Technology* **21** 045402 ISSN 0957-0233
[40] Wondrak T, Eckert S, Gerbeth G, Klotsche K, Stefani F, Timmel K, Peyton A, Terzija N and Yin W 2011 *Metallurgical and Materials Transactions B* **42** 1201–1210
[41] Ratajczak M, Gundrum T, Stefani F and Wondrak T 2014 *Journal of Sensors* **2014** 739161
[42] Ratajczak M, Gundrum T, Stefani F and Wondrak T 2015 *J. Manuf. Sci. Prod.* 41–48
[43] Ratajczak M, Wondrak T and Stefani F 2016 *Philosophical Transactions of the Royal Society A* **374**
[44] Timmel K, Eckert S, Gerbeth G, Stefani F and Wondrak T 2010 *ISIJ International* **50** 1134–1141
[45] Wondrak T an Pal J, Stefani F, Galindo V and Eckert S 2017 *Flow Measurement and Instrumentation* ArXiv: 1702.04880
[46] Matikainen L, Irons G, Morala E and Chang J S 1986 *Review of Scientific Instruments* **57** 1661–1666
[47] Banerjee S and Lahey Jr R 1981 *Advances in Nuclear Science and Technology* (Springer) pp 227–414
[48] Chang J S and Morala E 1990 *Nuclear Engineering and Design* **122** 143–156
[49] Moore P I, Brown G J and Stimpson B P 2000 *Measurement Science and Technology* **11** 1802
[50] Mahadeva D V, Baker R C and Woodhouse J 2009 *Instrumentation and Measurement, IEEE Transactions on* **58** 1602–1609
[51] Richter T, Keplinger O, Strumpf E, Wondrak T, Eckert K, Eckert S and Odenbach S 2017 *Magnetohydrodynamics* **53** 383–392
[52] Takeda Y 2012 *Ultrasonic Doppler velocity profiler for fluid flow* vol 101 (Springer)
[53] Vogt T, Andruszkiewicz A, Eckert S, Eckert K, Odenbach S and Gerbeth G 2012 *Metallurgical and Materials Transactions B* **43** 1454–1464
[54] Povolny A and Kikura H 2016 Ultrasound reflector recognition and tracking technique for two-phase flow *2016 24th International Conference on Nuclear Engineering* p V005T15A041
[55] Richter T, Eckert K, Yang X and Odenbach S 2015 *Nuclear Engineering and Design* **291** 64–70
[56] Terzija N, Yin W, Gerbeth G, Stefani F, Timmel K, Wondrak T and Peyton A J 2011 *Measurement Science & Technology* **22** 015501
[57] Wondrak T and Soleimani M 2017 *Measurement Science and Technology* **28** 064001
[58] Gundrum T, Büttner P, Dekdouk B, Peyton A, Wondrak T, Galindo V and Eckert S 2016 *Sensors* **16** 63
[59] Zürner T, Ratajczak M, Wondrak T and Eckert S 2017 *Measurement Science and Technology* Accepted